Experimental Investigation of an Algorithmic Approach for Optimizing DAB Converter Design

Rossano Mendes Sotoriva[1], **Mateus de Freitas Bueno**[1]**, Douglas Mendes Sotoriva**[1]**, Franciéli Lima de Sá**[2]**, Samir Ahmad Mussa**[1]

[1]Universidade Federal de Santa Catarina, Department of Electrical Engineering, Florianópolis – SC, Brazil.
[2]Facvest University Center, Lages, SC, Brazil.

e-mail: rossano.sotoriva@posgrad.ufsc.br; mateus.bueno@posgrad.ufsc.br; douglas.sotoriva@posgrad.ufsc.br; francielilimadesa@gmail.com; samir@inep.ufsc.br

ABSTRACT This study endeavors to optimize a dual active bridge (DAB) converter for seamless integration into an electric vehicle's on-board charger (OBC). The optimization process employs an algorithm to ascertain the optimal construction parameters, encompassing factors such as the number of turns in the inductor, gap length, and the number of turns in the primary and secondary windings of the transformer. By considering seven meticulously chosen operating points, the objective is to minimize the total loss sum and pinpoint the optimal frequencies for each point. Subsequently, a lookup table is formulated to ensure efficient OBC operation across varying output power and current levels by optimizing the frequency as a single variable. To validate the optimization process, the power switch losses are compared with theoretical calculations, and simulation results from PLECS 4.7.2 are leveraged. Furthermore, a prototype is meticulously assembled and tested to validate the DAB converter optimization, ultimately achieving an impressive efficiency of over 97%, thus affirming the efficacy of the optimization algorithm.

KEYWORDS Dual-Active Bridge, High-frequency magnetic, On-board charger, Optimum design.

Nomenclature

B_L	Density flux in the inductor
B_{trs}	Density flux in the transformer
EV	Electric vehicle
fs	Frequency
I_L	Inductor current
i_p	Primary current
i_s	Primary current
I_{sw}	Switching currents
i_{trs}	Transformer current
$iGSE$	Improved generalized Steinmetz equation
L	Inductance
l_g	Length of the inductor gap
N_L	Number of turns in the inductors
N_p	Number of turns in the primary
N_s	Number of turns in the secondary
NPZ	Non-Project Zone
OBC	On-board charger
p_k	Peak
P_o	Output power
RMS	Root mean square
V_i	Voltage input
V_o	Voltage output
ZVS	Zero voltage switching
ϕ	Phase-shift angle

I. INTRODUCTION

The global emphasis on reducing CO_2 emissions has driven the extensive adoption of electric vehicles (EVs) as a sustainable transportation alternative, with declining costs and better performances [1]. Nonetheless, the limited range of contemporary lithium-ion batteries poses a significant challenge to vehicle autonomy, highlighting the need for advancements in both battery technology and charging infrastructure [2].
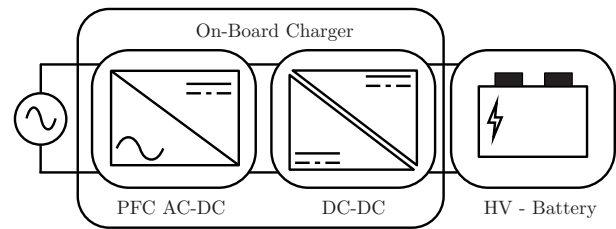
FIGURE 1. Basic on-board charger structure for electric vehicles.

The on-board charger (OBC) plays a crucial role in EVs by enabling direct battery recharging from the grid. While traditional OBCs support unidirectional power flow, bidirectional OBCs offer greater flexibility, allowing EVs to be utilized for various applications, such as vehicle-to-grid (V2G), vehicle-to-home (V2H), or vehicle-to-load (V2L) systems during idle periods [3].

The on-board chargers commonly consist of two conversion stages: power factor correction (PFC) and DC-DC

conversion, as illustrated in Figure 1. This study focuses specifically on the DC-DC stage, aiming to investigate the implementation and optimization of a DAB converter for integration into an OBC [4].

Power electronics must be efficient and supply electric power in a manner appropriate for user demands, typically through precisely regulated voltages or currents. With the progression of semiconductor technology and electronic packaging, along with growing demand across diverse sectors, the automated design and optimization of power electronic circuits have become increasingly vital. The strategies for automated synthesis and enhancement of these circuits are generally classified into deterministic and stochastic methods. deterministic techniques often encounter challenges such as being restricted to local optima due to the significant nonlinearity involved in power electronic circuits optimization.

These methods are also heavily influenced by the initial starting point of the search. Conversely, stochastic methods, including genetic algorithms and particle swarm optimization, are generally more effective for optimizing power electronic circuits. stochastic approaches explore the search space more comprehensively, avoid local optima, and provide more robust solutions through a more extensive exploration of possible configurations on the search space [5] [6].

As seen in [7] the DAB converter is being widely used on DC microgrids, and to achieve higher efficiency on the converter operation, optimization methods are being employed to reduce power or current stresses on the converter operation, since they can be utilized for parameters definition.

By reviewing the charging specifications of EVs currently on the market was established for this study a level-1 on-board charger [8].

II. DUAL ACTIVE BRIDGE - DAB

The DAB converter, as illustrated in the Figure 2, is a bidirectional converter capable of power transfer between its two bridges, it was chosen for this application due to its numerous advantages. These advantages include the utilization of a low number of components, zero voltage switching (ZVS) operation, and high flexibility with modulation schemes [9].
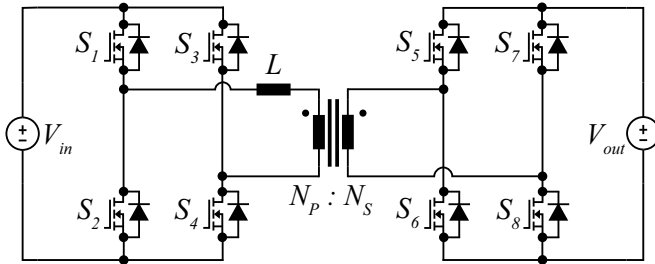

FIGURE 2. Dual Active Bridge (DAB) converter for use on DC-DC parcel of the on-board charger.

To control the power transfer in the DAB converter, various methods can be employed, such as adjusting the phase shift angle (ϕ) between the primary and secondary transformer voltages, modulating the duty cycle, or changing the switching frequency [10]. Among these methods, adjusting the phase shift angle is the most commonly used approach. For this particular work, a single phase shift with a variable frequency is chosen for controlling the power transfer.

III. LOSSES AND THERMAL MODELS

The loss model and thermal model employed in this study are presented on this section. Semiconductor losses are divided into two categories: switching losses and conduction losses.

Switching losses are computed based on the turn-on and turn-off energy characteristics as specified in the manufacturer datasheets for the switches. Conduction losses, conversely, are contingent upon the on-resistance (R_{ds-on}) of the switches and the RMS currents. Based of the flowchart exhibited on the Figure 3 the switching losses are calculated depending on the V_{bus} and I_{sw}.
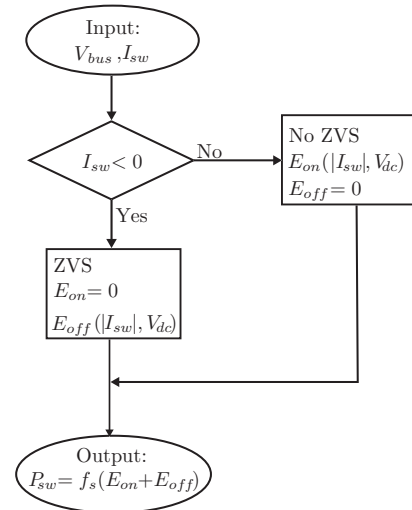
FIGURE 3. Switching loss flowchart.

It is possible to achieve ZVS on the switches turn-on, depending on the polarity of the inductor's current (i_L), as seen in [11]:

$$ZVS = \begin{cases} S_1, S_4, S_6, S_7 & = i_L < 0 \\ S_2, S_3, S_5, S_8 & = i_L > 0 \end{cases} \quad (1)$$

If the current of a switch is negative while being activated, Zero Voltage Switching (ZVS) will occur. The ZVS range for each phase shift can be acquired by the equations:

$$\begin{cases} \phi ZVS, pri > \frac{(d-1)}{d} \cdot \frac{\pi}{2} \\ \phi ZVS, sec > \frac{(1-d)\cdot \pi}{2} \end{cases} \quad (2)$$

where when the phase shift ϕ condition is true, ZVS is achieved at each side of the converter, the voltage ratio d is defined by,

$$d = n \cdot \frac{V_o}{V_i}. \tag{3}$$

Since the phase shift is proportional to the output power, the ZVS range can be plotted on an normalized output power over voltage ratio graph, as shown in Figure 4. The ZVS range can be further extended by applying different control schemes, such as extended-phase shift, dual-phase shift, or triple-phase shift control [12].
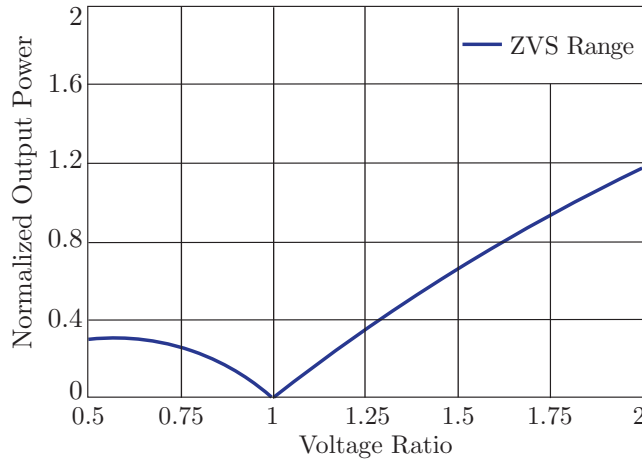

FIGURE 5. The BWM i3's theoretical charging profile is represented by a curve, and the operation points i to be optimized are indicated by square dots (■).

FIGURE 4. ZVS range with normalized output power over voltage ratio.

The DAB converter comprises two magnetic elements: the transformer and the inductor. Each of these elements incurs losses in their windings and cores. The core losses are calculated using the improved Generalized Steinmetz Equation (iGSE) [13]. As for the winding losses, Dowell equation is employed, which takes into account the resistance of the litz wire winding used in the magnetics [14]. Since these resistances are frequency-dependent, the Fourier series of the current is considered for the inductor, primary transformer, and secondary transformer. The thermal model employed in this study is based on [15]. It is important to note that this approach allows for the utilization of more sophisticated thermal models, such as those presented in [16].

IV. OPTIMUM DESIGN
To optimize the on-board charger, the battery pack configuration used is the 96s1p pack from the BMW i3, which consists of 96 Samsung SDI 94Ah cells in series, resulting in a total capacity of 33.6 kWh. The charging capacity is set to 0.1 C, equivalent to 9.4 A, resulting in a charging time of 10 hours. The charging profile can be seen in Figure 5, With the operation points indicated by square dots (■). The optimization process involves utilizing a particle swarm algorithm to find the optimal combination of parameters for N_{points} operation points, aiming to minimize the sum loss for all operation points.

Minimizing the operation points losses from the Figure 5 reduces charging load process losses. Increasing the number of points on the curve enhances accuracy but requires
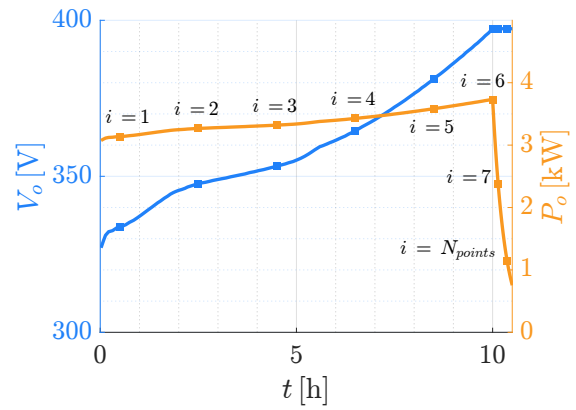
more computational calculation time. In order to adapt to the charging profile illustrated on the previous figure, an implemented modulation strategy allows precise adjustments to both the phase shift (ϕ) and the frequency (f_s) of the converter as can be seen in the DAB single phase shift power transfer equation given by

$$P(\phi, f_s) = \frac{V_i \cdot V_o \cdot \phi \cdot (\phi - \pi)}{2\pi^2 \cdot f_s \cdot L \cdot n} \tag{4}$$

with this approach is achieved a high level of flexibility, thereby enhancing the converter overall performance. It is essential to emphasize that power transfer within the DAB converter adheres to the formulation outlined in the equation above and directly impacts the converter operational efficiency. To measure the converter's gain, it will be optimized at both fixed and variable frequencies for result comparison.

This modulation capability facilitates the generation of the required PWM signal, subsequently controlling the power switches within the converter as can be seen in the Figure 6.
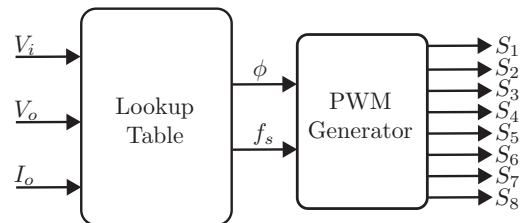
FIGURE 6. PWM generator based on lookup table.

The optimization process as shown in the Figure 7 involves the determination of four construction parameters at each operation point, namely: number of turns in the inductor (N_L), length of the inductor gap (l_g), number of turns in the primary (N_p) and number of turns in the secondary (N_s). It is assumed that there is no gap in the transformer. As there are multiple solutions for the converter, the routine finds the best possible combination for each operating point i, as shown in
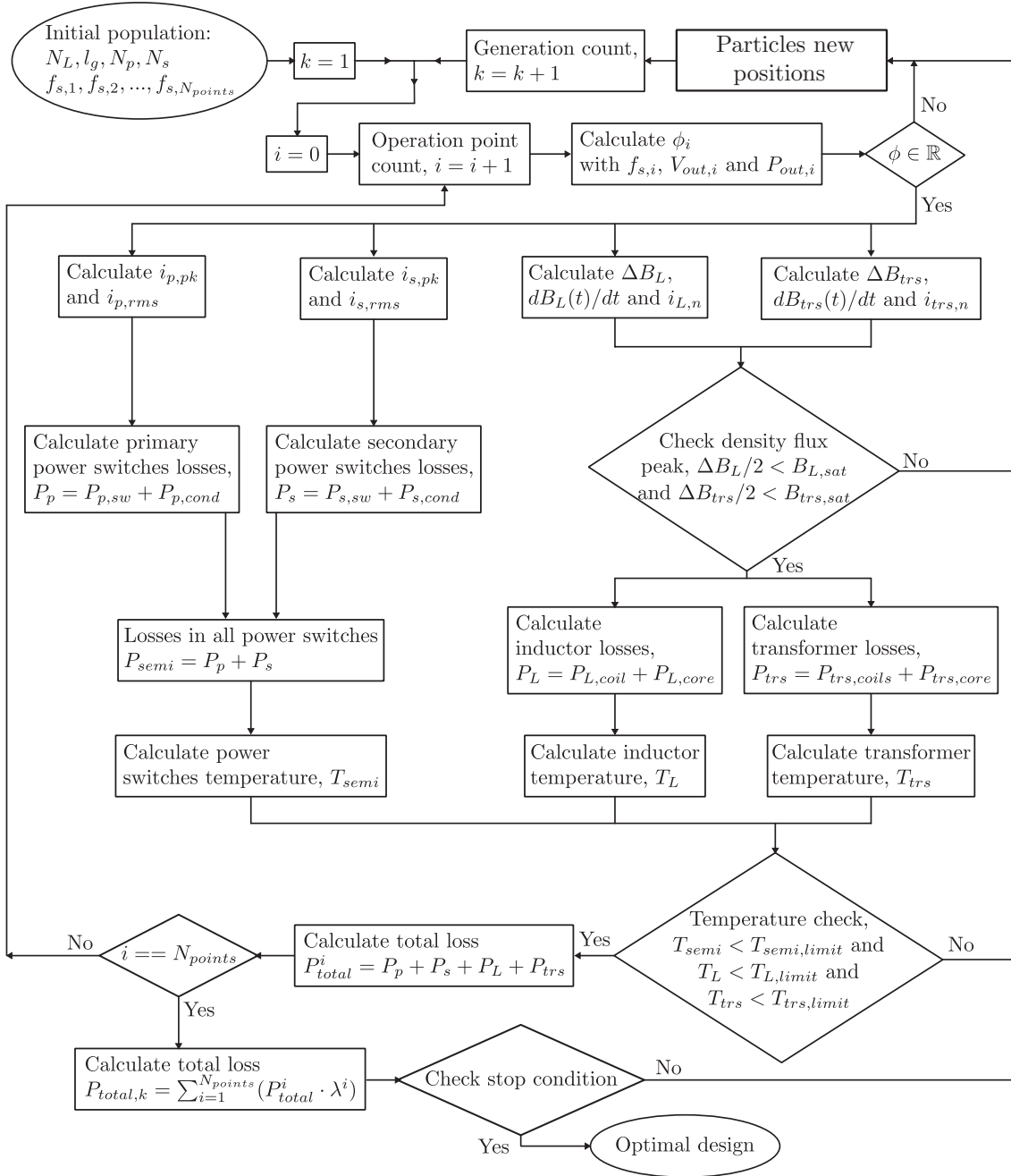
FIGURE 7. Design optimization flowchart for obtaining construction parameters.

Figure 5, a unique frequency ($f_{s,i}$) is selected as the variable to be optimized. In total, eleven parameters are used in the PSO algorithm for optimization in this work.

The hyperparameters used in the PSO algorithm for setting the optimization initial configuration are described in the Table 1,

where the swarm size used 300 particles per optimization variable, the max iterations were 200 with a max defined of stall iterations of 100, where if the algorithm do not find a better solution it ends the optimization early.

TABLE 1. Hyperparameters.

Hyperparameters	Value
Swarm Size	1500
Max Iterations	200
Max stall Iterations	100

The angle for each operation point i is calculated using a frequency ($f_{s,i}$), a output voltage ($V_{out,i}$) and a output power ($P_{out,i}$). Then, the following elements are calculated:

the peak current in the primary power switch ($i_{p,pk}$), the RMS current in the primary power switch ($i_{p,rms}$), the peak current in the secondary power switch ($i_{s,pk}$), the RMS current in the secondary power switch ($i_{s,rms}$), the peak-to-peak density flux in the inductor (ΔB_L), the derivative of the density flux in the inductor ($dB_L(t)/dt$), the inductor current in n^{th} harmonic ($i_{L,n}$), the peak-to-peak density flux in the transformer (ΔB_{trs}), the derivative of the density flux in the transformer ($dB_{trs}(t)/dt$), and the transformer current in ($i_{trs,n}$) at n^{th} harmonic. Using these values, it is possible to assess whether the magnetic elements saturate or if any element in the converter exceeds the temperature limit. If any of these conditions are met, the algorithm rejects the population, and the parameters undergo mutation before being retested.

V. DAB OPTIMIZATION

Initiating the optimization process involved establishing both upper and lower bounds for the population. These bounds are detailed in the accompanying Table 2.

TABLE 2. Optimization Limits.

Parameter	Lower Bounds	Upper Bounds
N_L	2	15
l_g	0.05 mm	2.0 mm
N_p	2	15
N_s	2	15
f_s	20 kHz	150 kHz

For the optimization process also were considered the materials detailed in Table 3, with all the specific characteristics of each one that are taken into account during the process.

TABLE 3. Material list.

Components	Code
Power switches	C3M0075120K
Heatsinks	LAM4K15012
Inductor core	E80/38/20-N87
Inductor wire	392x38AWG Litz
Transformer core	E80/38/20-N87
Transformer wires	392x38AWG Litz

Upon completion of the optimization process, the specifications for the DAB converter operating with a variable phase-shift and a fixed frequency can be acquired. At this stage, the construction parameters have undergone optimization with a fixed input voltage of 400 V. The results of the optimization process, are presented in Table 4.

As evident from the preceding table, both designs exhibit remarkable similarities in terms of construction, with only minor variations, resulting in similar efficiencies of 97.37% and 97.53%. The distinctions in inductor values between the two designs are also quite negligible. The most notable

TABLE 4. Optimum design summary.

	Fixed Frequency	Variable Frequency
$\bar{\eta}$	97.37%	97.53%
N_p	15	15
N_s	14	14
N_L	15	15
l_g	1.0 mm	1.1 mm
f_s	26.7 kHz	23.7 kHz to 50.2 kHz
L_{dab}	46.7 μH	44.7 μH
T_{semi-p}^{max}	50°C	50°C
T_{semi-s}^{max}	52°C	52°C
T_{tr}^{max}	121°C	121°C
T_L^{max}	67°C	65°C
B_{L-pk}^{max}	139 mT	139 mT
B_{tr-pk}^{max}	340 mT	278 mT

contrast between the two designs lies in their operating frequencies. The fixed frequency design maintains a constant frequency of 26.75 kHz, while the variable frequency design spans a range from 23.75 kHz to 50.21 kHz. When examining the efficiency of both converters at each operation point i, as shown in Figure 8, it becomes evident that both designs are viable. However, for the majority of the points, the configuration with variable frequency exhibits higher efficiency than the configuration with fixed frequency. While the results are promising, there is no way to guarantee that the converter will operate precisely according to the theoretical charging profile. To address this, a lookup table will be implemented to cover operation points that were not previously considered.

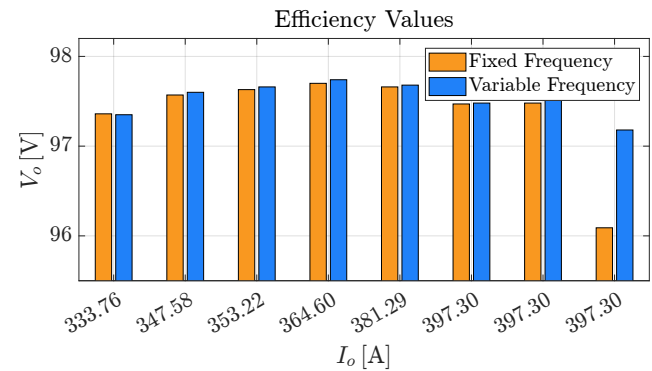**FIGURE 8.** Converters efficiency comparison operating with variable and fixed frequency.

VI. LOOKUP TABLE MODULATION SCHEME

To achieve the goal of designing a DAB converter capable of variable frequency operation across various profiles, as previously described, it becomes imperative to begin a second optimization phase. In this phase, a single variable, the frequency, is optimized for each step in voltage and power.

Given that only one parameter requires optimization at this stage, the process is executed relatively quickly.

During the second optimization process, the core principle involves the creation of a lookup table encompassing various combinations of output power and output current. The objective is to maximize converter efficiency for any V_o and I_o, even for points outside the charging profile. Each entry in this table specifies the optimal frequency, as shown in Figure 9, and the optimal phase-shift, depicted in Figure 10. Both figures demonstrate that utilizing these lookup tables enables the identification of numerous optimized operational points for the converter, extending beyond the initial eight points defined in Figure 5. Notably, these additional optimized points retain the fundamental characteristics of the charging profile, indicating the most suitable frequency range for each power output level.
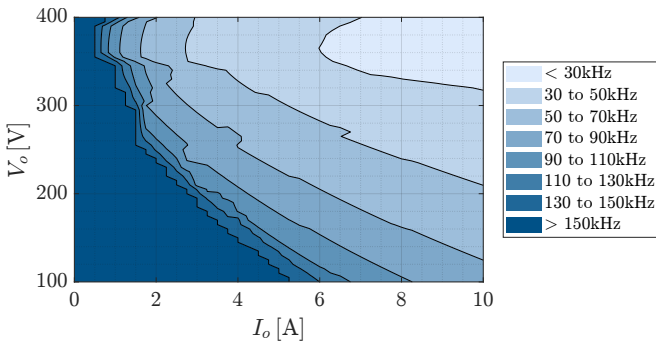

FIGURE 9. Frequency lookup table ranging between 30 kHz and 150 kHz

For better comprehension, contour lines based on the operation frequency were plotted in the Figure 9, delimiting the operation points for the desired V_o and I_o.
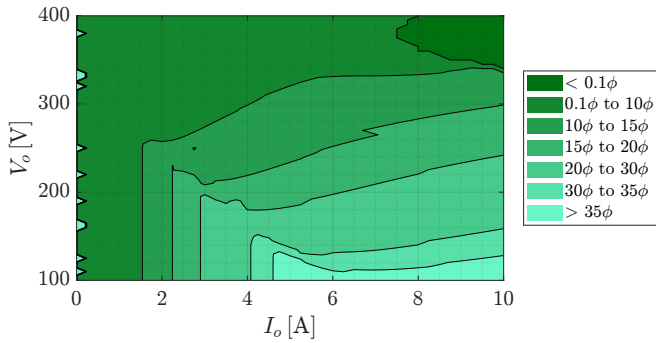

FIGURE 10. Phase-Shift lookup table ranging between 0 ϕ to 35 ϕ

Also for better comprehension, contour lines based on the phase-shift were plotted in the Figure 10, delimiting the operation points for the desired V_o and I_o.

When conducting a deeper comparison between the optimization processes for fixed and variable frequencies, while utilizing the same construction materials, several notable observations emerge from Figure 11. In cases where the

frequency remains fixed, the optimization outcomes align with the intended operational points. However, a distinctive pattern arises when operating at 200 V and 10 A: the final point showcasing at least 80% efficiency. Beyond this point, a significant region of the project exhibits zero efficiency; notably, regions below 180 V lack any viable operational points.
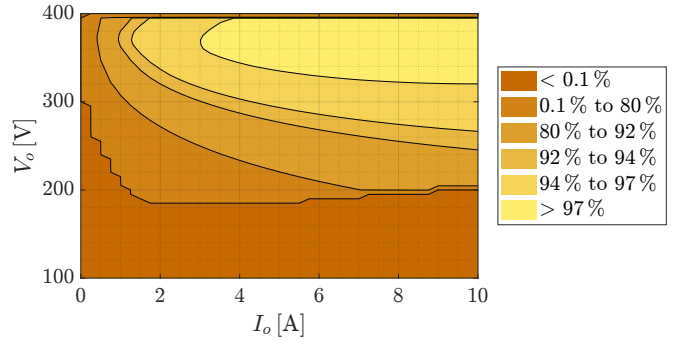

FIGURE 11. DAB efficiency map with fixed frequency ranging between 0% **to** 100%**.**

Upon analysing Figure 12, where the frequency (f_s) is variable, the results exhibit significantly more favorable trends, with a broader range of operating conditions showing higher efficiency. Notably, efficiencies can be identified for currents surpassing 2 A, even though they might be relatively modest. Especially notable is the attainment of an 80% efficiency with the converter operating at 150 V and 10 A. This outcome underscores the substantial benefits of employing variable frequency (f_s) optimization, which is considerably more compelling for vehicle charging applications.
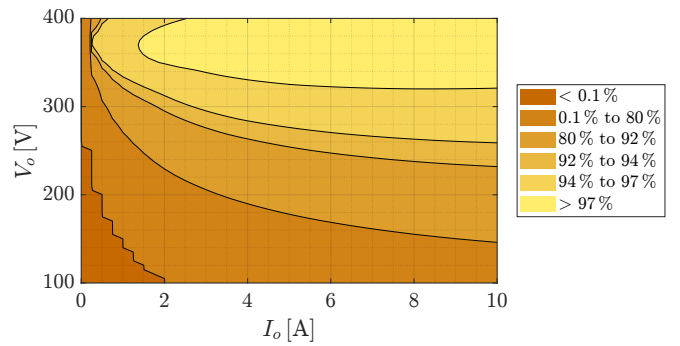
FIGURE 12. DAB efficiency map with variable frequency ranging between 0% **to** 100%**.**

VII. SIMULATION RESULTS OF THE PROPOSED OPTIMIZATION METHOD

To validate the optimization process, a comparison is conducted between theoretical (Thc) calculations and simulation (Sim) results obtained from PLECS 4.7.2. The error (Er), which represents the difference between these values, is used for comparison, affirming the accuracy and reliability of the

optimization process. Three distinct points of operation from the charging profile are selected for simulation, specifically points $i = 1$, 4, and 8, as shown in the Tables 5, 6 and 7.

TABLE 5. Results comparison for i = 1 (Vo = 333.77V).

Measurement	Thc. [W]	Sim. [W]	Er. [% - W]	
Pri. Switching Losses	3.70	3.42	7.56	0.28
Pri. Conduction Losses	14.46	14.52	0.41	0.06
Total Pri. Losses	18.16	17.94	1.21	0.22
Sec. Switching Losses	0.38	0.60	57.89	0.22
Sec. Conduction Losses	16.77	15.69	6.44	1.08
Total Secondary Losses	17.15	16.29	5.01	0.86
Total Switching Losses	35.31	34.23	3.05	1.08
Total Power Output	3137.4	3198.2	21.06	60.80

TABLE 6. Results comparison for i = 4 (Vo = 364.60V).

Measurement	Thc. [W]	Sim. [W]	Er. [% - W]	
Pri. Switching Losses	2.20	2.15	2.27	0.05
Pri. Conduction Losses	12.21	12.05	1.31	0.16
Total Pri. Losses	14.41	14.20	1.45	0.21
Sec. Switching Losses	1.91	1.91	0.00	0.00
Sec. Conduction Losses	14.17	13.49	4.79	0.68
Total Secondary Losses	16.08	15.40	4.22	0.68
Total Switching Losses	30.49	29.60	2.91	0.89
Total Power Output	3427.3	3418.2	0.26	9.10

TABLE 7. Results comparison for i = 8 (Vo = 397.31V).

Measurement	Thc. [W]	Sim. [W]	Er. [% - W]	
Pri. Switching Losses	0.09	0.00	99.17	0.09
Pri. Conduction Losses	1.59	1.54	3.14	0.05
Total Pri. Losses	1.68	1.54	8.33	0.14
Sec. Switching Losses	4.22	3.88	8.05	0.34
Sec. Conduction Losses	1.84	1.77	3.80	0.07
Total Secondary Losses	6.06	5.65	6.76	0.41
Total Switching Losses	7.74	7.19	7.10	0.55
Total Power Output	1139.4	1119.2	1.77	20.2

When considering the theoretical calculations, including magnetic losses, the results for all power losses are presented in Table 8. It is evident that all displayed points have achieved remarkable efficiency through the optimization algorithm, which considers variable ϕ and f_s for each situation.

TABLE 8. Charging Profile Results for i = 1,4 and 8.

P_o[W]	V_o[V]	I_o[A]	P_{losses}[W]	Efc[%]	f_s	ϕ
3137.4	333.77	9.4	85.95	97.26	27.54	10.324
3427.3	364.60	9.4	81.14	97.63	26.43	9.8834
1139.4	397.31	2.8	34.97	96.93	54.82	6.1173

VIII. THEORETICAL RESULTS

For the setting up experimental tests, the DAB converter was optimized using the same materials and optimization bounds as in previous studies, but with different objectives. The charging profile was modified and replaced by the profile detailed in Table 9, where all power outputs were consistently defined as 2 kW for each of the voltage outputs. This adjustment ensured uniform power delivery across varying voltage levels, allowing for a more controlled and consistent evaluation of the converter's performance under the new conditions.

TABLE 9. Charging profile of the experimental tests.

	V_i [V]	V_o [V]	P_o [W]
i = 1	400	300	2000
i = 2	400	350	2000
i = 3	400	400	2000
i = 4	400	450	2000

The optimization process was thus tailored to meet these specific requirements, ensuring the converter's efficiency and performance reliable across the revised operational profile. The new parameters of testing are as described in the Table 10.

TABLE 10. Optimum design theoretical results.

Parameter	Value
$\bar{\eta}$	97.37 %
N_p	12
N_s	14
N_L	14
l_g	0.52 mm

With this profile the optimized results provided for each operation point, a phase shift and an operational frequency have been defined through the optimization process, facilitating the desired power flow within the converter, as detailed in Table 11.

TABLE 11. Converter's frequency and phase shift - variable frequency.

	V_o [V]	f_s [kHz]	ϕ
i = 1	300	30.91	15.22
i = 2	350	34.01	14.28
i = 3	400	43.05	15.98
i = 4	450	61.54	20.94

After defining these values, it is possible to calculate the losses for each of the components optimized and estimate the overall losses of the converter.

A. Power switches losses

In the Table 12 can be seen the power losses for the switches each operation point.

TABLE 12. Power switch losses [W].

	$P_{sw,p}$	$P_{sw,s}$	$P_{cond,p}$	$P_{cond,s}$
i = 1	2.50	0.63	5.88	8.01
i = 2	2.32	2.33	4.12	5.62
i = 3	0.66	3.59	4.61	6.28
i = 4	0.32	6.42	5.05	6.87

An examination of the graphs in Figure 13 reveals that the conduction losses of the switches remain comparable to those observed in the fixed frequency optimization. Conversely, the switching losses are reduced, a result of the lower operating frequency.
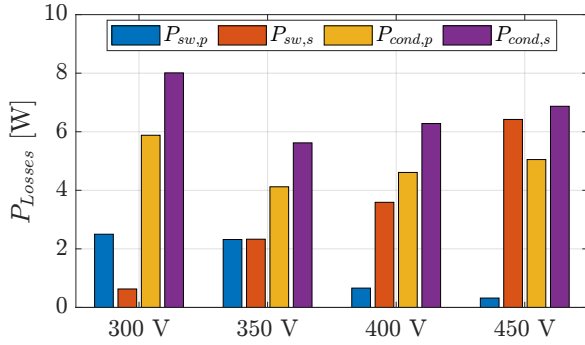

FIGURE 13. Switches power losses [W].

B. Magnetic elements losses

The results for the magnetic elements losses are exhibited on the Table 13.

TABLE 13. Magnetics elements power losses [W].

	$P_{ind,core}$	$P_{ind,cu}$	$P_{trs,core}$	$P_{trs,p,cu}$	$P_{trs,s,cu}$
i = 1	8.85	3.82	19.87	3.82	2.40
i = 2	4.11	3.29	25.78	3.29	2.07
i = 3	10.43	5.58	27.49	5.58	3.51
i = 4	18.97	11.78	24.82	11.78	7.42

The graphs in Figure 14 illustrate that transformer core losses increase with the variable frequency. However, other significant magnetic element losses, such as winding losses, are substantially lower due to the optimized frequencies for each operating point.
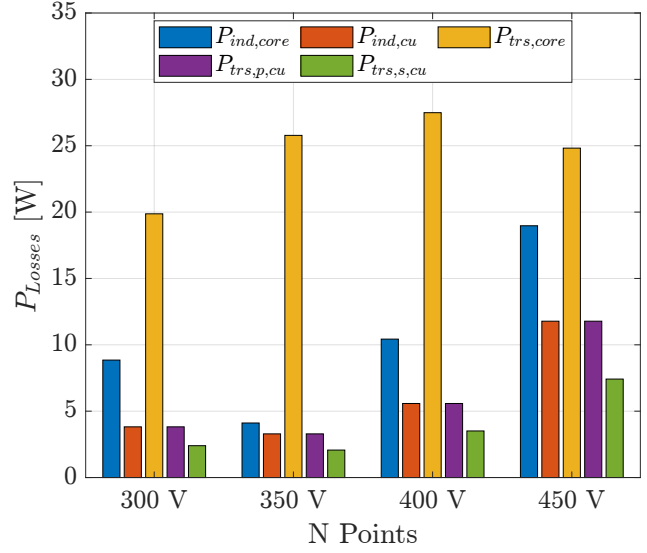

FIGURE 14. Magnetic elements power losses [W].

C. Converter theoretical efficiency

The graphs in Figure 15 illustrate that total losses at each operational point are reduced through variable frequency optimization, resulting in the converter achieving an efficiency of 96.55% at the 350 V point.
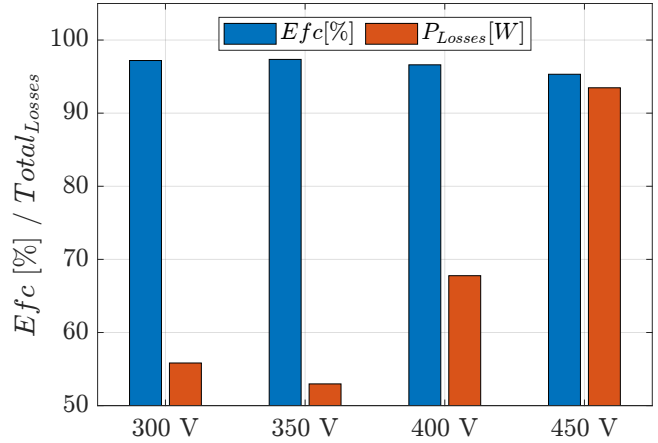

FIGURE 15. Theoretical converter's efficiency.

D. ZVS Range

In the figure 16, the Zero Voltage Switching (ZVS) regions for the primary side of the converter are illustrated, while Figure 17 showcases the ZVS regions for the secondary side of the converter under variable frequency conditions. Notably, for most of the operation points outlined in Table 9, ZVS is effectively achieved. However, it's worth mentioning that achieving ZVS at 300 V is unattainable under these conditions.

Another notable observation is the absence of the non-project zone (NPZ) in this scenario where the frequency is variable. Despite the higher switching losses associated with this approach, the overall losses of the converter are lower
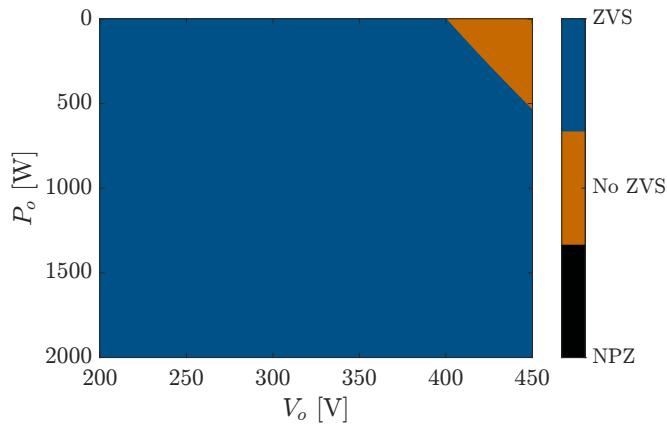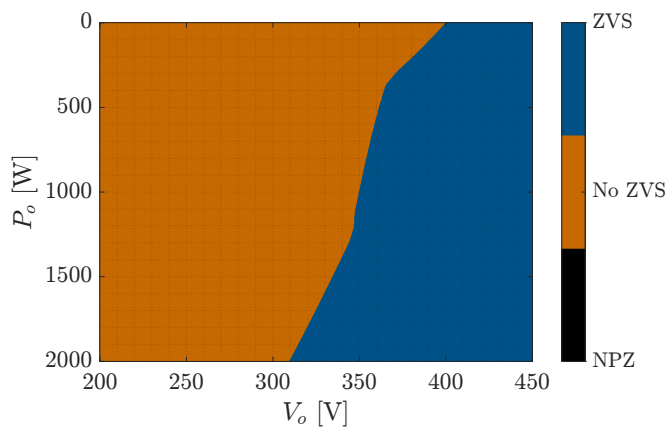
FIGURE 16. ZVS primary side.

FIGURE 17. ZVS secondary side.

due to the capability of operating at lower frequencies, thus contributing to higher efficiency.

IX. EXPERIMENTAL TESTS

A. Testing setup

The setup, depicted in the schematic in Figure 18, included a TS500-40 Programmable DC Power Supply as the voltage source (V_{in}) for the DAB converter. A resistive load (R_L) was connected at the converter's output to enable the measurement of input and output voltage, current, and power. The Yokogawa WT1800 precision power analyzer was used to measure these parameters at specified points.
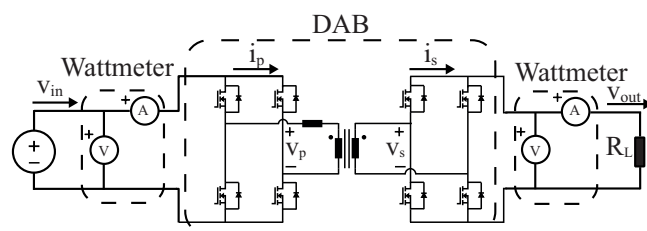

FIGURE 18. DAB test setup schematic.

To assess the transformer's primary and secondary, an oscilloscope was connected to the output of the primary bridge and the input of the secondary bridge. Specifically, a Tektronix MSO 3040 oscilloscope was utilized for this purpose. The physical prototype assembly is depicted in Figure 19.
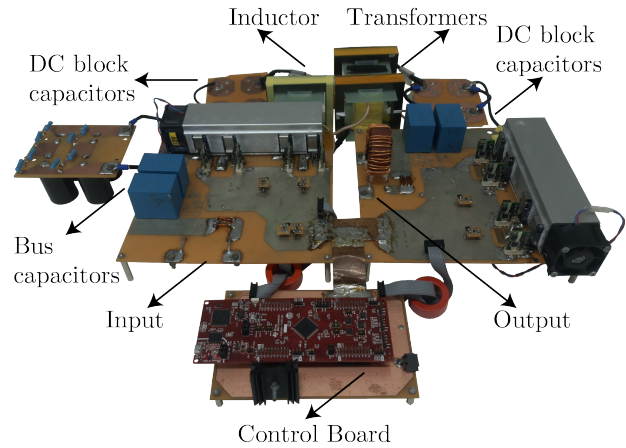

FIGURE 19. DAB converter prototype.

The Table 14, summarizes the results obtained on the experimental tests, presenting the output current, efficiency and power losses of each tested configuration.

TABLE 14. Experimental results.

Po[W]	Vo[V]	Io[A]	P_losses[W]	Efc[%]	f_s	ϕ
2000	300	6.30	63.64	96.85	30.91	15.22
2000	350	5.62	59.27	97.05	34.01	14.28
2000	400	4.87	74.57	96.34	43.05	15.98
2000	450	4.23	80.75	95.87	61.54	20.94

Figure 20 displays the waveforms illustrating current and voltage on both the primary and secondary sides of the converter during experimental tests. On the primary side, a peak current of 8.93 A and -9.40 is observed, accompanied by overvoltage peaking at 519 V and -452 V.

Conversely, the secondary side exhibits conspicuous peaks of overcurrent and overvoltage whenever a switch transitions, with the current peaking at 11.26 and -12.59 A, with the voltage peaks being 321.15 V and -330.38 V. Additionally, the converter's dead time manifests as a discernible effect on the secondary side, wherein the voltage briefly drops to zero during these intervals. This phenomenon is less pronounced on the primary side due to the presence of the inductor and the capacitance of the switches, which discharge during the dead time, thus maintaining voltage levels on the primary side.

Figure 21 depicts the waveforms illustrating current and voltage on both the primary and secondary sides of the converter during experimental tests. On the primary side, a peak current of 6.83 A and -6.64 A was observed, accompanied by an overvoltage peaking at 460.18 V and -427.79 V.
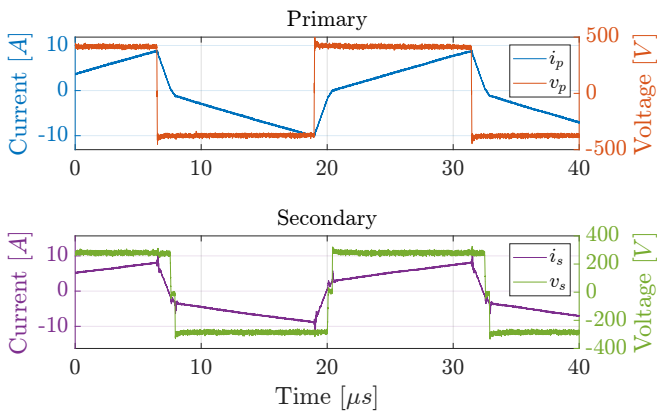
FIGURE 20. Converter's primary and secondary waveforms - 300 V.

On the secondary side, notable peaks of overcurrent and overvoltage were observed during each switching event, with the current spiking at 15.53 A and -15.16 A, with the voltage reaching a peak of 429.12 V and -442.89 V. Similar to the previous test, transient periods were observed where the voltage level momentarily dropped to zero on the secondary side.
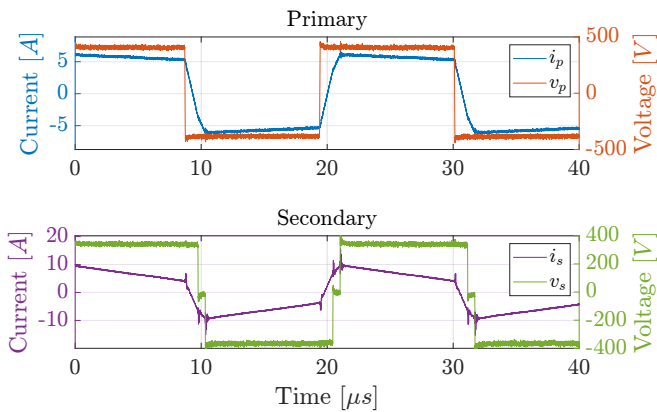

FIGURE 21. Converter's primary and secondary waveforms - 350 V.

In Figure 22, the waveforms depicting current and voltage on both the primary and secondary sides of the converter during experimental tests are presented. Notably, the peak current observed is +8.81 A and -9.10 A on the primary side, accompanied by voltage levels peaking at 426.92 V and -433.07 V.

On the secondary side, noticeable peaks of overcurrent and overvoltage are observed during switching events, with the current reaching a peak of 19.56 A and -19.95 A, with the voltage peaking at 534.83 V and -485.16 V. Similar to previous tests, there is a brief period where the voltage level remains at zero on the secondary side.

Figure 23 illustrates the waveforms of current and voltage on both the primary and secondary sides of the converter during experimental tests. Notably, a peak current of 9.43
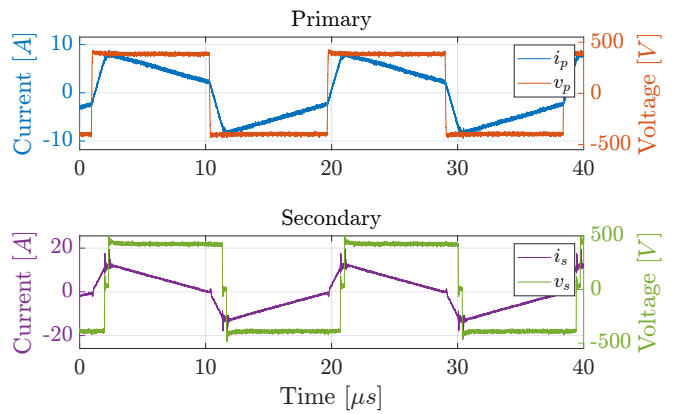

FIGURE 22. Converter's primary and secondary waveforms - 400 V.

A and -10.20 A was observed on the primary side, accompanied by voltage levels reaching a peak of 477.56 V and -450.45 V. At this operational point, a distinct phenomenon is observed where the voltage levels on the primary side momentarily drop to zero, attributed to the dead time effect. It's important to highlight that at this specific operational point, the switching frequency is essentially twice that of the initial operational point. This implies reduced time for energy storage on the primary side, leading to an instant where no voltage is present.

Similarly, on the secondary side, peaks of overcurrent and overvoltage are evident during converter operation. The observed current peak is 21.40 A and -23.51 A, and the voltage peak reaches 601.89 V and -520.11 V. Once again, a brief period of zero voltage levels is observed on the secondary side, as seen in previous tests.
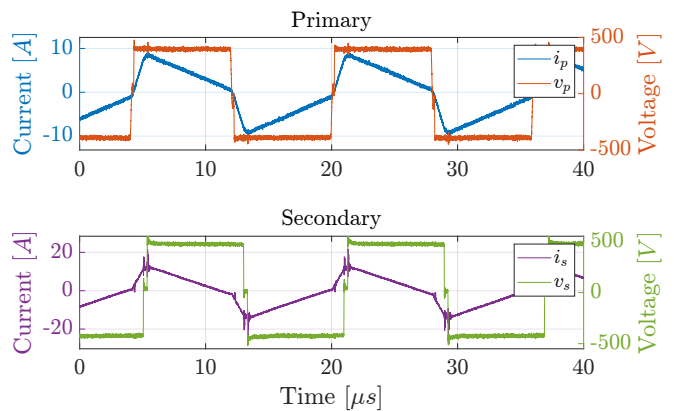

FIGURE 23. Converter's primary and secondary waveforms - 450 V.

The results obtained demonstrate a minimal margin of error between the intended values and those observed in testing. Notably, the 350 V results exhibit the highest efficiency, while the 450 V result represents the lowest. Nonetheless, all achieved outcomes are deemed satisfactory, meeting the objective of optimizing a converter for various operational

points encompassing different frequencies and phase shifts. Importantly, each case demonstrates an efficiency exceeding 95%, as can be observed in Figure 24, underscoring the success of the optimization approach employed.
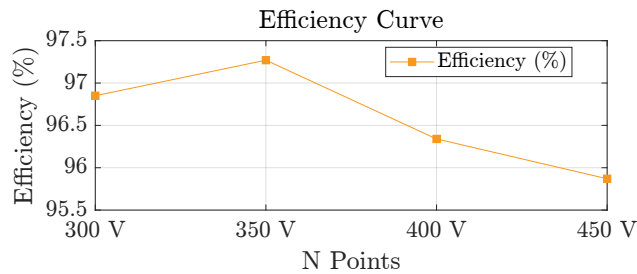

FIGURE 24. Comparative converter efficiency curve of each tested point.

X. CONCLUSION

Based on the obtained results, the effectiveness of the optimization process becomes evident. This iterative approach allows for the continuous refinement of the converter design, utilizing the available construction parameters to ensure the best possible assembly for optimization, suitable for an onboard charger application. The challenge of this methodology lies in the calculation of losses and the unique construction characteristics of each topology. Nevertheless, the algorithm can be easily adapted since it has a modular structure, making it applicable to the study of various converter topologies.

Operation points for optimizing the converter established a suitable voltage range and power output for OBC applications. The flexibility of the optimization methodology was highlighted, demonstrating its applicability to different converters and applications by focusing on minimizing total losses. The results confirmed the effectiveness of this optimization process, with satisfactory outcomes across all tested scenarios. The iterative approach showed how continuous refinement using available construction parameters could achieve optimal designs, making the methodology highly relevant for onboard chargers and other IBDC applications.

The positive results underscore the potential for further advancements and optimizations in the field. The iterative optimization process, with its focus on minimizing losses and adapting to various topologies, offers a robust framework for future research and development. The demonstrated success in achieving high efficiency and low losses across different operational points confirms the viability and effectiveness of the proposed optimization strategy, paving the way for more efficient and reliable power electronic converters in various applications.

AUTHOR'S CONTRIBUTIONS

SOTORIVA, R. M., BUENO, M. F., SOTORIVA, D. M., DE SÁ, F. L., MUSSA, S. A.: Conceptualization, Data Curation, Formal Analysis, Funding Acquisition, Investigation, Methodology, Project Administration, Resources, Software, Supervision, Validation, Visualization, Writing – Original Draft, Writing – Review & Editing.

REFERENCES

[1] M. Muratori, M. Alexander, D. Arent, M. Bazilian, P. Cazzola, E. M. Dede, J. Farrell, C. Gearhart, D. Greene, A. Jenn, M. Keyser, T. Lipman, S. Narumanchi, A. Pesaran, R. Sioshansi, E. Suomalainen, G. Tal, K. Walkowicz, J. Ward, "The rise of electric vehicles—2020 status and future expectations", *Progress in Energy*, vol. 3, no. 2, p. 022002, mar 2021, doi:10.1088/2516-1083/abe0ad.

[2] C. Liu, K. T. Chau, D. Wu, S. Gao, "Opportunities and Challenges of Vehicle-to-Home, Vehicle-to-Vehicle, and Vehicle-to-Grid Technologies", *Proceedings of the IEEE*, vol. 101, no. 11, pp. 2409–2427, 2013, doi:10.1109/JPROC.2013.2271951.

[3] S. Kampl, *Topologies in on-board charging*, Infineon, 2020.

[4] K. Fahem, D. E. Chariag, L. Sbita, "On-board bidirectional battery chargers topologies for plug-in hybrid electric vehicles", *in 2017 International Conference on Green Energy Conversion Systems (GECS)*, pp. 1–6, 2017, doi:10.1109/GECS.2017.8066189.

[5] J. Zhang, Y. Shi, Z.-H. Zhan, "Power Electronic Circuits Design: A Particle Swarm Optimization Approach", *in* X. Li, M. Kirley, M. Zhang, D. Green, V. Ciesielski, H. Abbass, Z. Michalewicz, T. Hendtlass, K. Deb, K. C. Tan, J. Branke, Y. Shi, eds., *Simulated Evolution and Learning*, pp. 605–614, Springer Berlin Heidelberg, Berlin, Heidelberg, 2008.

[6] Y. Shi, R. C. Eberhart, "Parameter selection in particle swarm optimization", *in* V. W. Porto, N. Saravanan, D. Waagen, A. E. Eiben, eds., *Evolutionary Programming VII*, pp. 591–600, Springer Berlin Heidelberg, Berlin, Heidelberg, 1998.

[7] Y. Deng, S. Yin, J. Chen, W. Song, "A Comprehensive Steady-State Performance Optimization Method of Dual Active Bridge DC-DC Converters Based onWith Triple-Phase-Shift Modulation", *in 2022 IEEE International Power Electronics and Application Conference and Exposition (PEAC)*, pp. 221–225, 2022, doi:10.1109/PEAC56338.2022.9959445.

[8] M. Safayatullah, M. T. Elrais, S. Ghosh, R. Rezaii, I. Batarseh, "A Comprehensive Review of Power Converter Topologies and Control Methods for Electric Vehicle Fast Charging Applications", *IEEE Access*, vol. 10, pp. 40753–40793, 2022, doi:10.1109/ACCESS.2022.3166935.

[9] F. Krismer, *Modeling and optimization of bidirectional dual active bridge DC-DC converter topologies*, Doctoral thesis, ETH Zurich, Zürich, 2010, doi:10.3929/ethz-a-006395373, diss., Eidgenössische Technische Hochschule ETH Zürich, Nr. 19177, 2010.

[10] F. Krismer, J. W. Kolar, "Accurate small-signal model for an automotive bidirectional Dual Active Bridge converter", *in 2008 11th Workshop on Control and Modeling for Power Electronics*, pp. 1–10, 2008, doi:10.1109/COMPEL.2008.4634699.

[11] A. Rodríguez, A. Vázquez, D. G. Lamar, M. M. Hernando, J. Sebastián, "Different Purpose Design Strategies and Techniques to Improve the Performance of a Dual Active Bridge With Phase-Shift Control", *IEEE Transactions on Power Electronics*, vol. 30, no. 2, pp. 790–804, 2015, doi:10.1109/TPEL.2014.2309853.

[12] L. Song, H. Ramakrishnan, N. Kumar, M. Bhardwaj, *Bidirectional, Dual Active Bridge Reference Design for Level 3 Electric Vehicle Charging Stations*, Texas Instruments, Dallas, Texas, 2022.

[13] W. Hurley, W. Wölfle, *Transformers and inductors for power electronics: theory, design and applications*, Wiley, Hoboken, NJ, 2013, URL: http://cds.cern.ch/record/1616895.

[14] S. Geng, M. Chu, W. Wang, P. Wan, X. Peng, H. Lu, P. Li, "Modelling and optimization of winding resistance for litz wire inductors", *IET Power Electronics*, vol. 14, no. 10, pp. 1834–1843, 2021.

[15] M. K. Kazimierczuk, "High-Frequency Magnetic Components: Second Edition", *High-Frequency Magnetic Components: Second Edition*, pp. 1–729, 11 2013, doi:10.1002/9781118717806.

[16] B. Bertoldi, "Systematic procedures for the design of passive components applied to a high performance three-phase rectifier", , 2021.

BIOGRAPHIES

Rossano Mendes Sotoriva Born in Vacaria, Rio Grande do Sul, Brazil, in 1997. He received his Bachelor's degree in Electrical Engineering from the Centro Universitário Facvest (Unifacvest) in 2021 and its master's degree in Power Electronics at the Federal University of Santa Catarina (UFSC) in 2024, currently pursuing a Phd degree in Power Electronics at the Federal University of Santa Catarina (UFSC). His areas of interest are: Power electronics, DC-DC converters and converters optimization.

Mateus de Freitas Bueno Graduated in Electrical Engineering from the State University of Santa Catarina - UDESC (2020/2). He was a member and scholarship holder of the PET Electrical Engineering Group at UDESC from March 2016 to July 2019. During this period, he completed scientific initiation for 2 years in the area of statistics and biomedicine. In addition, he also participated in teaching and extension projects aimed at technical, social and administrative development. He completed a supervised internship at WEG Drives and Controls, focused on developing firmware for automatic voltage regulators. Received its master's degree in Power Electronics at the Federal University of Santa Catarina (UFSC) in 2023. Currently working on the private sector.

Douglas Mendes Sotoriva Born in Vacaria, Rio Grande do Sul, Brazil, in 1997. He received his Bachelor's degree in Electrical Engineering from the Centro Universitário Facvest (Unifacvest) in 2020 and is currently pursuing a Master's degree in Power Electronics at the Federal University of Santa Catarina (UFSC). His areas of interest are: Power electronics

Franciéli Lima de Sá holds a degree and master's degree in Electrical Engineering from the State University of Santa Catarina - (UDESC, 2008 and 2010) respectively, a PhD in Electrical Engineering from the Federal University of Santa Catarina - (UFSC, 2014). She is currently Coordinator of the Electrical Engineering Course at Centro Universitário Facvest (UNIFACVEST). He has experience in the Power Electronics area, working mainly in the following lines: dc-dc converters, control applied in power electronics, FPGA-based systems. Dr. Franciéli is a member of the Brazilian Society of Power Electronics (SOBRAEP).

Samir Ahmad Mussa , He received the degree of Electrical Engineer from the Federal University of Santa Maria in 1988, he received the Master's and Doctor's degrees from the Federal University of Santa Catarina in 1994 and 2003 respectively. He currently holds the position of Full Professor in the Department of Electrical and Electronic Engineering (EEL) at the Federal University of Santa Catarina (UFSC) and researcher at the Institute of Power Electronics (INEP). His research interests include PFC rectifiers, digital signal processing and control applied in power electronics, DSP-based systems, FPGA and microprocessors. Dr. Mussa is a member of the Brazilian Society of Power Electronics (SOBRAEP) and the IEEE.

12

Eletrônica de Potência, Rio de Janeiro, v. 29, e202444, 2024.